

Heavy ion irradiation effects on CrFeMnNi and AlCrFeMnNi high entropy alloys



Youxing Chen^{a,b}, Di Chen^{c,d}, Jordan Weaver^{a,e}, Jonathan Gigax^a, Yongqiang Wang^c, Nathan A. Mara^{a,f}, Saryu Fensin^c, Stuart A. Maloy^c, Amit Misra^{g,*}, Nan Li^{a,*}

^a Center for Integrated Nanotechnologies, Los Alamos National Laboratory, Los Alamos, NM 87545

^b Department of Mechanical Engineering and Engineering Science, University of North Carolina, Charlotte, NC 28223

^c MST-8, Los Alamos National Laboratory, Los Alamos, NM 87545

^d Department of Physics, Texas Center for Superconductivity, University of Houston, Houston, TX 77204

^e Current affiliation: National Institute of Standards and Technology: Engineering Laboratory, Gaithersburg, MD 20899

^f Department of Chemical Engineering and Materials Science, University of Minnesota, Minneapolis, MN 55455

^g Department of Materials Science and Engineering, and Department of Mechanical Engineering, University of Michigan, Ann Arbor, MI 48109

ARTICLE INFO

Article history:

Received 21 March 2022

Revised 29 October 2022

Accepted 18 November 2022

Available online 24 November 2022

ABSTRACT

Co-free but Al-included medium/high entropy alloys (M/HEAs) have gained increasing interests due to their lower cost and the potential to tune the multi-phase microstructure. The irradiation response of two Co-free HEAs, face-centered cubic (FCC) CrFeMnNi with limited Cr enriched α' phase and body-centered cubic (BCC) AlCrFeMnNi with B2 s phase and nanoprecipitates were explored. Ion irradiations using 5 MeV Fe²⁺ ions were performed at 500 °C to a peak fluence of 50 and/or 100 displacements per atom (dpa). In dual-phase AlCrFeMnNi, there was no significant radiation induced segregation or chemical intermixing at the coherent matrix (FeCrMn-rich)/second phase (AlNi-rich) boundaries. In CrFeMnNi, limited voids were only detected at the peak damage location of ~ 50 dpa. On the other hand, voids were widely distributed in AlCrFeMnNi: under 50 and 100 dpa irradiation conditions, voids were found with larger dimension and denser distribution in the FeCrMn-rich matrix, smaller and slightly lower density in an AlNi-rich second phase. In addition, the diameter of the FeCMn-rich nanoprecipitates didn't reveal any tendency of dissolution or growth. This is correlated with their superior structural stability against irradiation. Significant radiation-induced hardening (increases from 3.8 ± 0.2 GPa to 4.7 ± 0.6 GPa) was measured in CrFeMnNi, but only ~ 4% hardness increase (from 7.4 ± 0.8 GPa to 7.7 ± 0.4 GPa) was noted in AlCrFeMnNi. In addition to the radiation-induced defects, such as voids, dislocation loops and point defects, other factors, such as chemical short-range ordering may play an important role.

© 2022 Published by Elsevier B.V.

1. Introduction

The need for more efficient, passively safe, and transportable nuclear reactors has been promoted, and this poses a challenge for the understanding of ion-solid interactions and material design for radiation damage tolerance [1–3]. This is because the service environments of nuclear materials are extremely harsh [4,5]: a combination of high temperatures, large time-varying stresses, chemically reactive environments, and intense neutron radiation fields. Further, radiation damage is not an isolated problem but a collection of inter-related damage modes that lead to material failure in very different ways. Under irradiation, large excess concentrations of vacancy and interstitial defects (Frenkel pairs) are cre-

ated and cause complex microstructural and microchemical evolution, including the accumulation of extended vacancy and interstitial defect clusters, nonequilibrium solute segregation, radiation-enhanced and -induced precipitation, and dimensional swelling. A host of performance-sustaining material properties are significantly degraded by these microstructural-microchemical changes induced by irradiation [5].

Medium/high entropy alloys (M/HEAs), composed of three or more metallic elements mixed in equal or near-equal atomic fractions in single-phase microstructures, exhibit excellent mechanical properties [6–13], resistance to helium bubble growth [14–17], and enhanced radiation tolerance [7,18–21] making these alloys potential candidates for structural applications in high-temperature fission and fusion reactors. Increasing chemical disorder in single-phase M/HEAs leads to a substantial reduction in electron mean free path [22]. Such localized electron-electron interactions cause a prolonged thermal spike and increase in electronic temperature in

* Corresponding authors.

E-mail addresses: amitmisi@umich.edu (A. Misra), nanli@lanl.gov (N. Li).

the vicinity of the collision cascades. Hence, during the process of radiation bombardments, a strong tendency of recombination between vacancies and interstitials is expected, and the number of survived Frenkel pairs is found to be significantly less as compared to pure metals [23]. Similarly, intrinsic severe lattice distortion, as a consequence of the random distribution of several different sized atoms in the crystal lattice, effectively suppresses the defect diffusion process and leads to magnified vacancy-interstitial recombination volume [24,25]. Consequently, the aggregation of radiation-induced defects may be slowed down [26–29].

Radiation-induced segregation (RIS) is also commonly reported in multiple chemical element alloys under radiation environments. During irradiation, vacancies and interstitials flow towards the grain boundaries. Due to the varied diffusion rates and bonding strength with vacancies, elements are either depleted or enriched near grain boundaries. However, RIS in HEAs can be mitigated due to the suppressed defect mobility. Previous irradiation studies have demonstrated that although irradiation led to the grain boundary segregation of Cr and V in W-based HEAs [20] and Ni and Co in Ni-based HEAs [29–32], the magnitude of RIS in irradiated HEAs was significantly lowered.

Currently, many HEAs are mainly developed based on CoCrNi using 3d transition elements. In this study, CrFeMnNi and AlCr-FeMnNi were selected due to the reasons as follows: First, for potential nuclear energy and high-temperature applications of HEAs, the amount of Co should be avoided (it is easily activated under irradiation). Second, it was reported that the addition of Al could transform FCC structure into dual-phase structure of BCC matrix and B2 ordered second phase [33–35]. The interface between BCC matrix and B2 s phase may be tolerant against ion irradiation in terms of segregation and decomposition due to its low energy [36–40]. Meanwhile, the difference in radiation tolerance of matrix and B2 is also worth exploring.

2. Experimental

Equiatomic CrFeMnNi and AlCrFeMnNi were produced by Sophisticated Alloys Inc. Specimens were cast and followed by consolidation via hot isostatic pressing (HIP) with a pressure of 100 MPa at 1200 °C for four hours. 5 MeV Fe²⁺ ion irradiations were performed using the NEC 3 MV Pelletron Tandem Ion Accelerator in the Ion Beam Materials Laboratory (IBML) at LANL. The specimens were irradiated at 500 °C to a peak influence of 50 and 100 dpa, which were calculated using the “Quick Calculation of Damage” option in SRIM (the Stopping and Range of Ions in Matter [41]). A displacement energy of 40 eV was used. Note that for materials development for advanced nuclear reactors, 500 °C is often selected for radiation studies [42], facilitating comparisons with other studies at the same temperature [19]. Transmission electron microscopy (TEM) samples were prepared in a FEI Helios Nanolab DualBeam. An FEI Tecnai F30 TEM operating at 300 kV was used for the examination of radiation-generated voids and correlated chemical distribution before and after irradiation, in which TEM point-to-point resolution is 0.21 nm and scanning TEM (STEM) resolution is 0.34 nm. Here, the energy-dispersive X-ray spectrometry (EDS) line scan under TEM was performed in high-angle annular dark-field (HAADF) STEM mode with the spatial resolution less than 0.5 nm. The minimum mass fraction detectable under alignment was estimated to be on the order of one half of one atomic percentage. In addition, the thickness of the TEM foil was measured using electron energy loss spectroscopy (EELS) plasmon technique. EEL spectra were collected at multiple locations between 400 nm ~ 1000 nm beneath the irradiated surface. The average foil thickness is 40 ± 8 nm. Nanohardness was measured using Bruker/Hysitron 950 TribolIndenter with standard Berkovich diamond tip and the method of load control to a final displace-

ment depth of 100 nm ~ 400 nm. For each sample, 10 by 10 indentation pattern has been applied. The Oliver-Pharr method [43] was used to calculate the hardness value.

3. Results

3.1. Microstructure of as-received HEAs

As shown in Fig. 1, CrFeMnNi HEAs have a polycrystalline FCC structure, in which Cr-rich but Ni-depleted BCC α' precipitates randomly distribute. The detailed information was reported in [44,45]. The addition of Al modifies the microstructure to a dual-phase structure with BCC and B2 phases. Fig. 2a presents the electron-backscatter diffraction (EBSD) inverse pole figure (IPF) orientation map of the equiatomic AlFeCrNiMn, which shows a polycrystalline structure with an average grain size of ~ 40 μm (Fig. 2b). Fig. 2c is the correlated energy-dispersive X-ray spectrometry (EDS) mapping within one typical grain. A characteristic structural feature of spinodal decomposition is presented with an oscillated composition profile [46]. Al and Ni enriched B2 phase is segregated from the FeCrMn-rich matrix but shares the same crystallographic orientation as the matrix. Similar microstructures have also been reported in the other Al-contained HEAs [47,48], as well as in ternary Ni-Fe-Al alloys [49].

In order to clarify the internal microstructure, a TEM foil was lifted out at a grain boundary and examined by high-angle annular dark-field (HAADF)-scanning TEM (STEM) (Fig. 3a). The second phase inside grains are labeled by the yellow dashed lines (Fig. 3b). In Fig. 3b', a representative EDS line scan is performed across the second phase/matrix interface, confirming the FeCrMn-rich matrix with a Al and Ni enriched second phase. Magnified STEM image in Fig. 3c uncovered the nanosized spherical particles with a size of 20 - 50 nm distributed inside the second phase. The correlated EDS line scan in Figs. 3c and 3c' shows Fe, Cr, and Mn enrichment of the nanoparticles. A high-resolution TEM image is taken at the boundary of the FeCrMn-rich matrix and AlNi-rich second phase to present the coherent interface. The inset diffraction pattern (DP) confirms no crystallographic orientation deviation between the matrix and the internal second phase throughout the whole grain. It is noted that separate microstructural studies regarding similarly composed HEAs have been reported [34,50]. A slight difference in dendrite distribution is probably due to the different fabrication routes.

3.2. Irradiation damage in CrFeMnNi HEA

5 MeV Fe ion irradiation at 500 °C with a peak damage level of 50 dpa was performed at LANL. Limited voids were found only

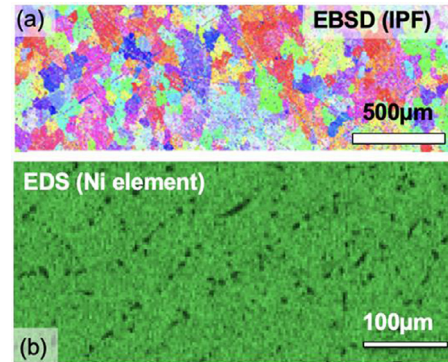


Fig. 1. SEM micrographs of as-received FeCrNiMn HEA. (a) EBSD IPF map shows a polycrystalline structure with a mean grain size of ~24 μm . (b) EDS map demonstrates that inside the grain, Cr-rich but Ni-depleted BCC precipitates are commonly seen. More information is shown in [45].

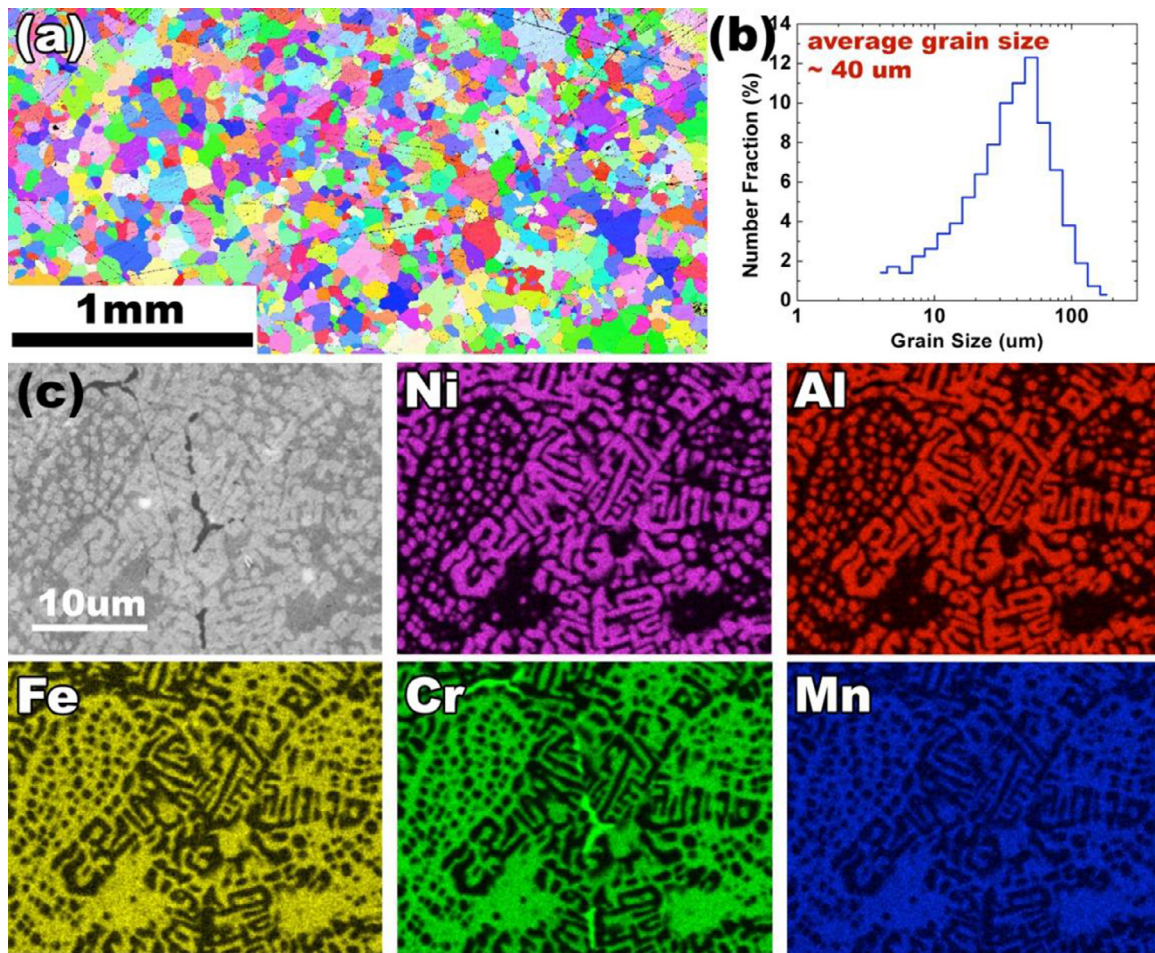


Fig. 2. (a) EBSD inverse pole figure map of the HIPed AlCrFeMnNi base material. (b) Grain size distribution to reveal the average grain size is $\sim 40 \mu\text{m}$. (c) EDS mapping in one grain to uncover the chemical element distribution. Al and Ni were segregated inside the Fe, Cr, Mn-rich matrix.

at the peak damage locations ($1.2 - 1.5 \mu\text{m}$ beneath, as shown in Fig. 4b). The average void size and density here is approximately 6 nm and $1.5 \times 10^{21}/\text{m}^3$, respectively. Meanwhile, irradiation at this condition didn't lead to any precipitation, which is consistent with other studies of Ni ion irradiation at elevated temperature on a similar alloy composition [31]. In addition, ref. [31] pointed out that no voids were observed in CrFeMnNi after irradiation up to a dose of 10 dpa [31]. This indicates that CrFeMnNi is resistant to precipitation under irradiation and there is a threshold dose for void nucleation lies between 10 and 50 dpa .

3.3. Microstructure evolution in irradiated AlCrFeMnNi HEA

The microstructural evolution of dual-phase AlCrFeMnNi HEA under the same irradiation conditions is shown in Fig. 5. Fig. 5a is the bright-field TEM image with overlapped SRIM simulated dpa vs. depth profile. Fig. 5b shows a magnified under-focused TEM image at $\sim 600 \text{ nm}$ beneath the surface (corresponding to $\sim 15 \text{ dpa}$), with voids appearing as bright dots surrounded by a dark Fresnel fringe. Voids are heterogeneously distributed in the FeCrMn-rich matrix and AlNi-rich second phase. The extent of aggregation at the matrix/second phase boundary is negligible here. The histogram for corresponding void size distribution in matrix (red) and second phase (blue) is shown in Fig. 5b'. Here, the average void size is $7.7 \pm 2.8 \text{ nm}$ in matrix, and $3.5 \pm 0.6 \text{ nm}$ in second phase grains. Measured by EELS, the average thickness of the TEM foil is $\sim 40 \text{ nm}$. The correlated void density at such

a location is $\sim 4.5 \times 10^{21} \text{ m}^{-3}$ in the FeCrMn-rich matrix (red) and $8.9 \times 10^{20} \text{ m}^{-3}$ in the AlNi-rich second phase (blue). In addition, nanoparticles with opposite contrast features are also shown without any hint of decomposition. Fig. 5c is the TEM image at $\sim 1.3 \mu\text{m}$ beneath the surface, which corresponds to the peak damage level ($\sim 50 \text{ dpa}$). The density of probed voids here is $\sim 1 \times 10^{22} \text{ m}^{-3}$ in matrix and $\sim 4.1 \times 10^{21} \text{ m}^{-3}$ in the second phase. The correlated size distribution shown in Fig. 5c' uncovers a similar trend: larger voids in the matrix phase (the average void size is $8.3 \pm 2.5 \text{ nm}$ in matrix, and $4.5 \pm 1.1 \text{ nm}$ in second phase grains). The initial second phase/matrix boundary is still retained after irradiation in all regions. Figs. 5d and 5e are the EDS line scans across the second phase/matrix boundaries at $\sim 600 \text{ nm}$ and $1.3 \mu\text{m}$ beneath the surface, respectively. After irradiation to $\sim 50 \text{ dpa}$, no chemical segregation is found at the coherent FeCrMn-rich matrix/AlNi-rich second phase boundaries.

When the peak radiation damage was increased to 100 dpa , it was observed that the overall microstructure was still maintained without nucleation of new phases. Fig. 6a shows the cross-sectional TEM image of irradiated AlCrFeMnNi HEA. From separated DPs on the respective matrix and second phase, no amorphization was detected and nanoprecipitates maintained their crystallinity under irradiation to 100 dpa . The correlated EDS line scan across two Fe, Cr, Mn-rich nanoprecipitates in Al, Ni-rich second phase at $\sim 1000 \text{ nm}$ beneath (corresponding to a dpa of ~ 60) uncovered the chemical distribution across the interface. The nanoscale particles maintained their identity without any indica-

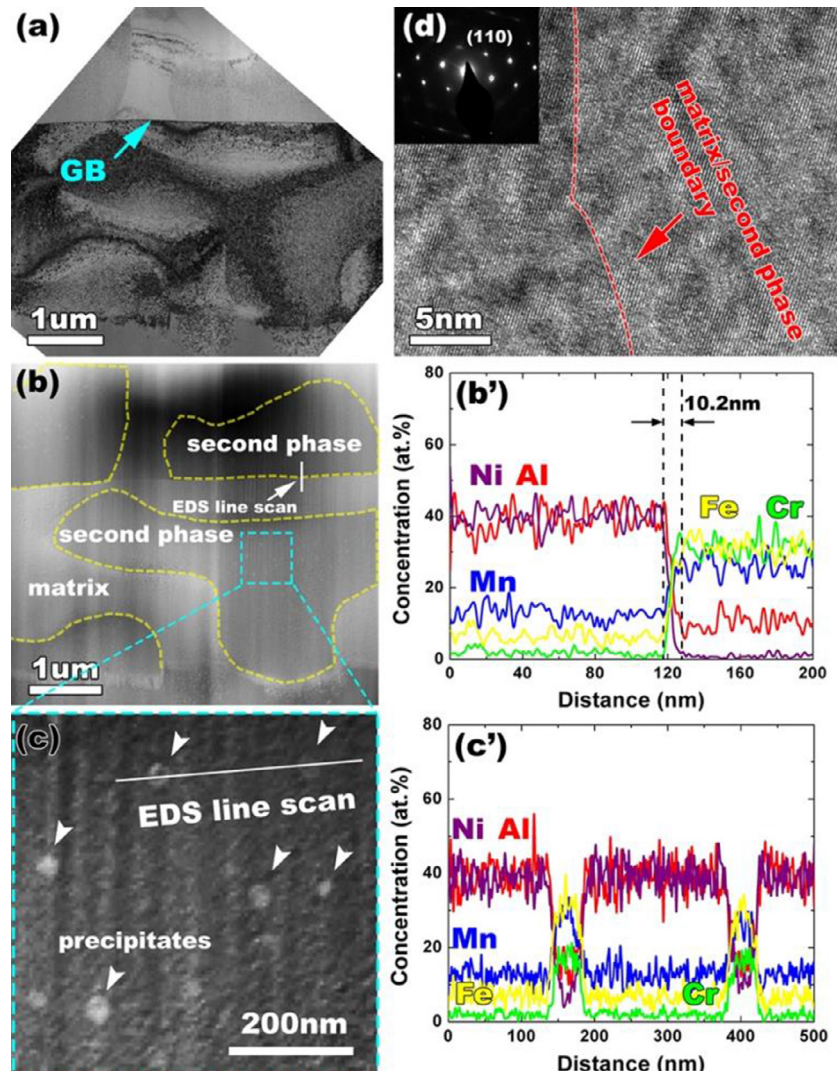


Fig. 3. (a) Cross-sectional TEM and (b) corresponding HAADF-STEM micrographs of HIPed AlCrFeMnNi base material. (b') a representative EDS line scan across the Al, Ni-rich second phase/ Fe, Cr, Mn-rich matrix interface. (c) magnified HAADF-STEM image in precipitate to uncover the existence of spherical nanoparticles. (c') EDS line scan across the nanoprecipitates to identify the enrichment of Fe, Cr and Mn. (d) The high-resolution TEM image taken at the coherent second phase/matrix interface with inset selected area diffraction pattern.

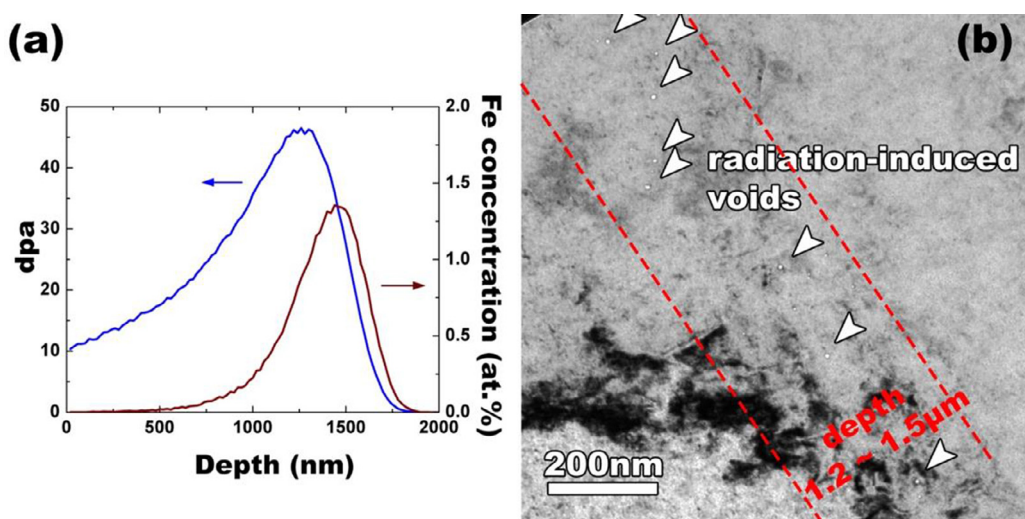


Fig. 4. (a) SRIM dpa and implanted Fe concentration profiles as a function of the irradiation depth. (b) TEM image of irradiated CrFeMnNi.

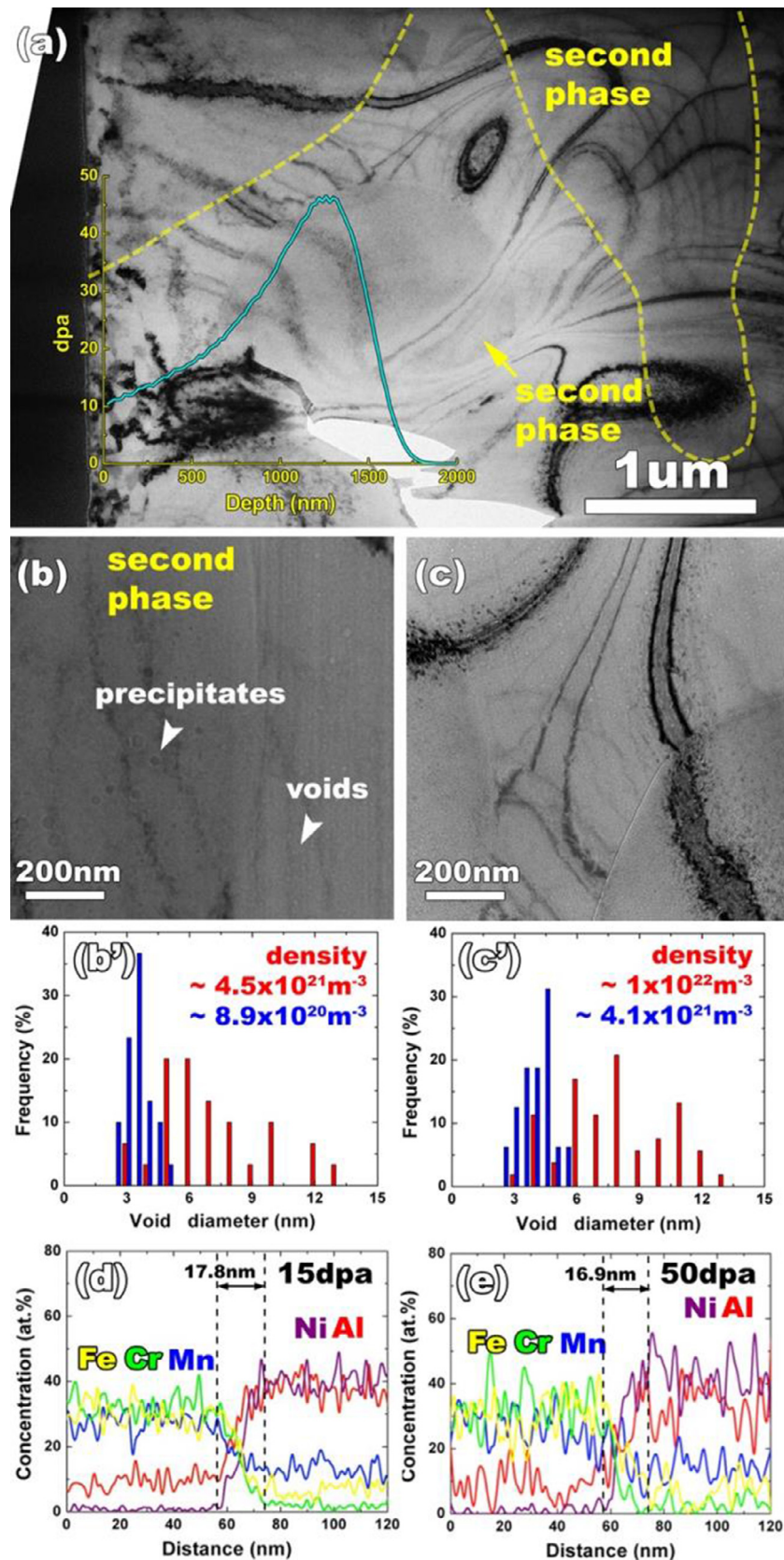


Fig. 5. (a) Cross sectional TEM image of irradiated AlCrFeMnNi HEA to a peak influence of 50 dpa with overlapped SRIM calculation. (b) and (c) Magnified under focused TEM images at ~600 nm and 1.3 μm beneath the surface, respectively. (b') and (c') are corresponding void size distribution in Fe, Cr, Mn-rich matrix (red) and Al, Ni-rich second phase (blue), respectively. (d) and (e) are the EDS line scans across the second phase/matrix boundaries at ~600 nm and 1.3 μm beneath the surface, respectively.

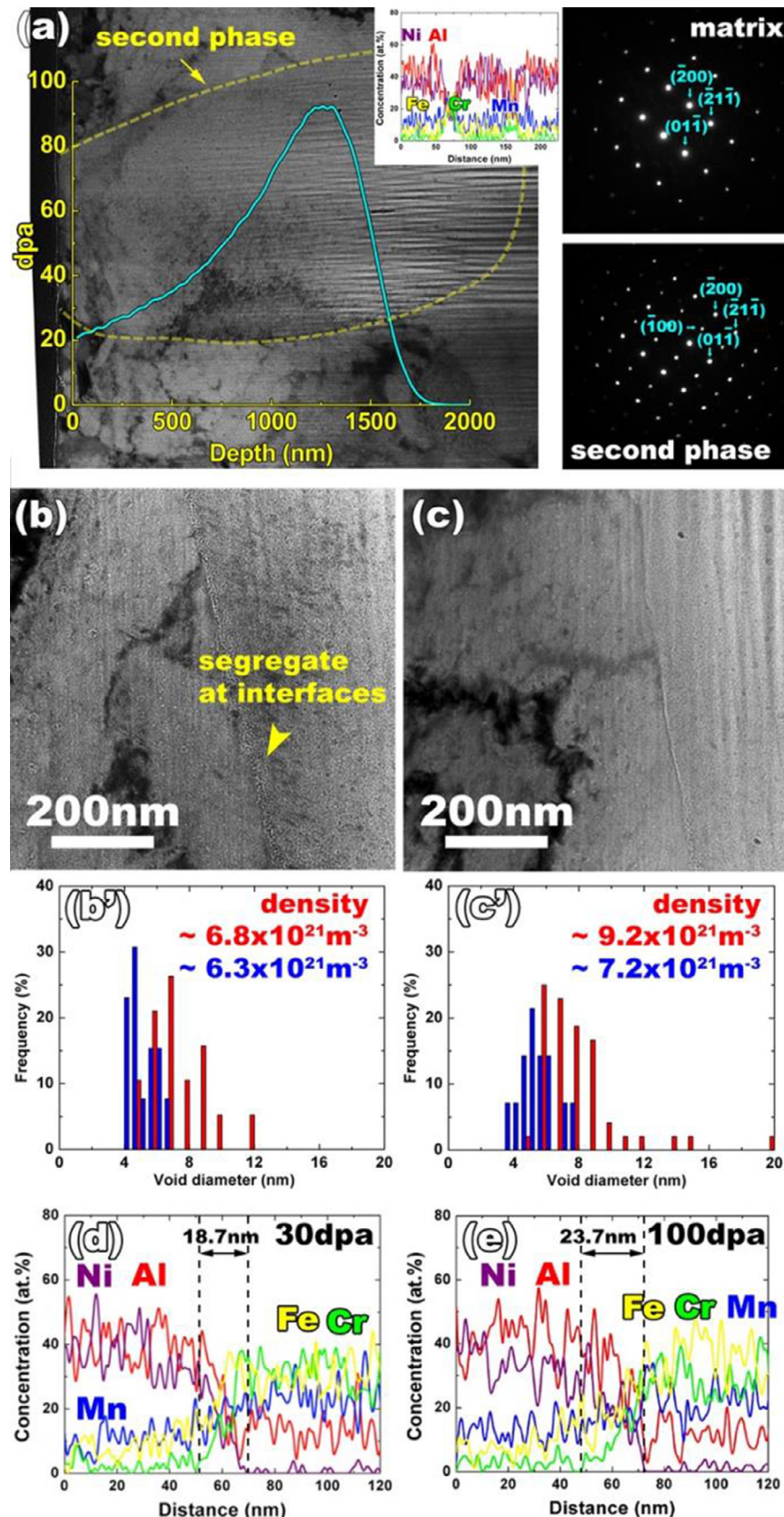


Fig. 6. (a) Cross-sectional TEM image of irradiated AlCrFeMnNi HEA to a peak influence of 100 dpa. The calculated SRIM profile is overlaid in the image. Inset is the EDS line scan across two Fe, Cr, Mn-rich nanoprecipitates in the Al, Ni-rich second phase at ~1000 nm beneath the surface. (b) and (c) Magnified under focused TEM images at ~600 nm and 1.3 μm beneath the surface, respectively. (b') and (c') are corresponding void size distribution in Fe, Cr, Mn-rich matrix (red) and Al, Ni-rich second phase (blue), respectively. (d) and (e) are the EDS line scans across the second phase/matrix boundaries at respective correlated depths beneath the surface.

Table 1

Nanohardness measurements of CrFeMnNi and AlCrFeMnNi before and after irradiation.

	As-received	50 dpa irradiated	100 dpa irradiated
CrFeMnNi	3.8 ± 0.2 GPa	4.7 ± 0.6 GPa	N/A
AlCrFeMnNi	7.4 ± 0.8 GPa	7.7 ± 0.4 GPa	7.8 ± 0.6 GPa

tion of amorphization or dissolution. Figs. 6b and 6c are the magnified micrographs at 600 nm and 1.3 μm beneath the surface, respectively. Corresponding statistical analysis of void size and density in matrix and second phases are presented in Fig. 6b' and 6c'. In comparison to the irradiation situation shown in Fig. 5, the void size doesn't change much: the average void size is 7.8 ± 1.7 nm in matrix, 4.9 ± 0.8 nm in second phase in Fig. 6b', and 8.2 ± 2.7 nm and 5.2 ± 1.2 nm in Fig. 6c', respectively. Figs. 6d and 6e are the EDS line scans performed across the Fe, Cr, Mn-rich matrix/Al, Ni-rich second phase boundary at respective depths. The measured chemical profile of the interface tends to be widening slightly with increased irradiation dose, from 10.2 nm (Fig. 3b') before irradiation to 18.7 nm at 30 dpa (Fig. 6b) and 23.7 nm at 100 dpa (Fig. 6e). This may be due to the cascade-induced ballistic displacements during irradiation, as previously reported radiation-induced chemical intermixing in Ni-based superalloys [51,52].

3.4. Nanohardness change after irradiation

Nanoindentation was performed to assess radiation-induced hardness changes (as shown in Table 1). In CrFeMnNi, hardness increases from 3.8 ± 0.2 GPa to 4.7 ± 0.6 GPa (24% increase by 0.9 GPa) after irradiation to a dose of 50 peak dpa at 500 °C. In AlCrFeMnNi, hardness changes from 7.4 ± 0.8 GPa to 7.7 ± 0.4 GPa (only 4% increase by 0.3 GPa) under the same irradiation condition, and to 7.8 ± 0.6 GPa with a dose of 100 peak dpa. Generally, the magnitude of hardening resulting from glide dislocations interacting with radiation-induced defects (like voids here) can be estimated by the Orowan model: $\Delta\sigma = M\alpha\mu b/\sqrt{Nd}$, where M represents the Taylor factor, α the barrier strength, μ the shear modulus, b the Burgers vector, N the void density, and d the void diameter [53–58]. For the case of irradiated CrFeMnNi, we take the Taylor factor of 3.06 [59], barrier strength of 1 for voids [50,60], shear modulus of 87 GPa (average from chemical composition), lattice parameter of 3.6 Å (based on TEM DP measurement and consistent with ref. [35]), void diameter of 5 nm, and density of $1.5 \times 10^{21}/\text{m}^3$ (value at peak damage region). The upper bound of a void-induced hardness increase is approximately 0.5 GPa. Thus, limited voids alone cannot account for the measured hardening and other strengthening mechanisms must be involved. These could be radiation induced dislocation loops, or the change of chemical short-range ordering [61–63], both of which were not investigated in this study. On the other hand, for AlCrFeMnNi irradiated to a dose of 50 peak dpa, we take the shear modulus of 91 GPa (average from chemical composition), void diameter of 8 nm, and average density of $4.5 \times 10^{21} \text{ m}^{-3}$ for Fe, Cr, Mn-rich matrix; and 72 GPa, 4 nm and $9 \times 10^{20} \text{ m}^{-3}$ for Al, Ni-rich second phase. For both phases, lattice parameter is taken as 2.9 Å (based on TEM DP measurement and consistent with ref. [34]). The calculated hardness increase is approximately 0.79 GPa, much higher than the measurement. Thus, softening mechanisms might occur during radiation to compensate the hardening, such as the change of short-range ordering and slight chemical intermixing. The results here indicated that radiation-induced structural changes in HEAs are more complex than conventional alloys.

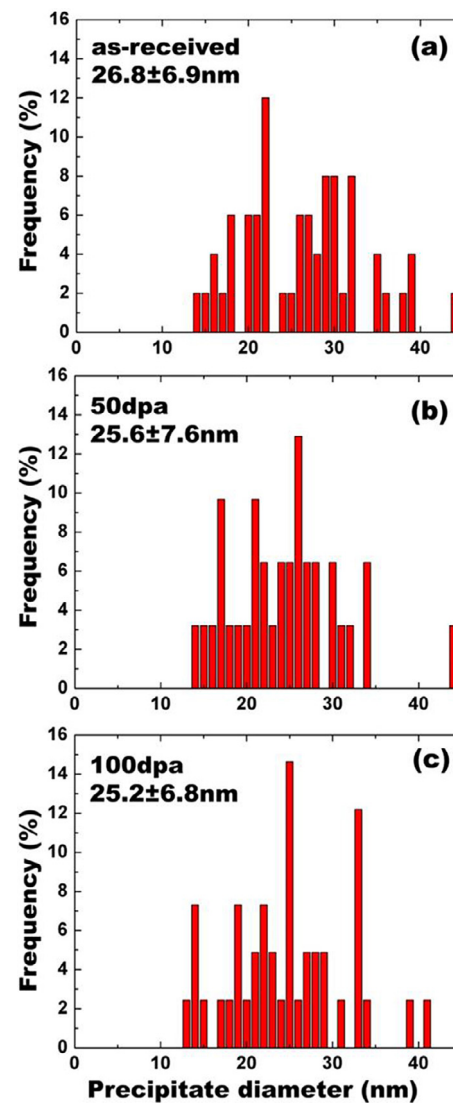


Fig. 7. Measurements of nanoprecipitate size in as-received, 50 dpa irradiated and 100 dpa irradiated Al, Ni-rich second phases, respectively.

4. Discussion

4.1. Phase stability after irradiation

Both alloys exhibited extraordinary phase stability under ion irradiation. As discussed in the [24], alloy complexity from high entropy alloys reduces defect mobility and alters defect migration paths on a modified energy landscape. As a result, the annihilation of radiation damage (vacancy – interstitial recombination) is promoted, and radiation tolerance is enhanced. The stability of AlCrFeMnNi subjected to irradiation is of particular interest as this HEA has a complex microstructure that potentially enhances radiation tolerance. There are three phases in AlCrFeMnNi: a FeCrMn-rich matrix, an AlNi-rich second phase, and FeCrMn-rich nanoprecipitates in the second phase. As shown in Figs. 5 and 6, no clear indication of interdiffusion or segregation was observed at interfaces between matrix and second phase, demonstrating good stability. Additionally, the nanoprecipitates also demonstrated great structural stability. First, they maintained crystallinity with no amorphization observed. Second, as shown in Fig. 7, these precipitates retained their dimensions of 25–27 nm (diameter) without dissolution or growth in irradiated AlCrFeMnNi (50 and 100 peak

Table 2

The composition of nominal CrFeMnNi, AlCrFeMnNi and measured in matrix and second phase in AlCr-FeMnNi.

	Al	Cr	Fe	Mn	Ni	Entropy (S)	Lattice distortion (δ)
CrFeMnNi	–	0.25	0.25	0.25	0.25	1.39R*	0.017
AlCrFeMnNi (designed)	0.2	0.2	0.2	0.2	0.2	1.61R	0.047
Matrix	0.1	0.3	0.3	0.3	–	1.31R	0.031
Second Phase	0.4	0.03	0.07	0.1	0.4	1.25R	0.062

* R is gas constant.

dpa). This further indicates that AlCrFeMnNi has superior structural stability against irradiation.

In comparison, the stability of the precipitates under irradiation has been a challenge in Ni-based superalloys. At room temperature, the submicron-sized γ' in Ni-based superalloy Rene N4 became fully disordered at ~ 0.3 dpa and partially dissolved after 75 dpa irradiation [51]. At high temperature, γ' precipitates tend to grow: e.g., they could grow to ~ 550 nm at 600 and 800 °C in Ni-based Oxide Dispersion-Strengthened (ODS) superalloys subjected to 100 dpa irradiation [64]. According to Nelson-Hudson-Mazey (NHM) model, precipitate growth is dominant at high temperature in nickel-base alloys [65]. The superior stability of nanoprecipitates in AlCrFeMnNi might be ascribed to the limited diffusion and further study is required to clarify the mechanism.

4.2. Void size and density in different irradiated phases

Detailed void information in irradiated CrFeMnNi and AlCr-FeMnNi HEAs has been described previously. Under the same irradiation conditions (at 50 peak dpa), the void size in irradiated the FeCrMn-rich matrix phase tends to be larger than those in the AlNi-rich second phase or CrFeMnNi FCC phase: ~ 8 nm in Fe, Cr, Mn-rich matrix, ~ 6 nm in CrFeMnNi and ~ 4 nm in AlNi-rich second phase. The void density in CrFeMnNi is lower ($1.5 \times 10^{21} m^{-3}$) than that in AlCrFeMnNi, specifically $\sim 1 \times 10^{22} m^{-3}$ in matrix and $\sim 4.1 \times 10^{21} m^{-3}$ in second phase. Therefore, the matrix in AlCrFeMnNi shows the highest void density and largest void size. The second phase in AlCrFeMnNi shows a higher void density but smaller void size than CrFeMnNi. To explore this, compositional complexity (entropy) and lattice discussion are discussed.

Generally, the compositional complexity has shown a positive effect on void suppression. Note that AlCrFeMnNi consists of two phases: the matrix is enriched with Fe (~30%), Cr (~30%), and Mn (~30%); the second phase is enriched with Ni (~40%) and Al (~40%). The configurational entropy (S) and lattice distortion (δ) can be calculated as:

$$S = -R\sum c_i \ln c_i \quad (1)$$

$$\delta = \sqrt{\sum_{i=1}^N c_i \left(1 - r_i / \sum_{j=1}^N c_j r_j\right)^2} \quad (2)$$

where c_i and r_i are the chemical concentration and atomic size of each element. Here are the parameters we are using: Ni – 1.25 Å; Mn – 1.31 Å; Cr – 1.29 Å; Fe – 1.29 Å, which are calculated from atomistic simulations and experiments [66]; and Al – 1.43 Å from [7].

As shown in Table 2, due to the segregation in AlCrFeMnNi, the matrix and second phase in AlCrFeMnNi have lower entropies than CrFeMnNi. That might explain the lower radiation resistance of the matrix of AlCrFeMnNi, although the lattice distortion is higher in the matrix. On the other hand, the second phase shows smallest void size, which might be due to the highest lattice distortion and ordered B2 structure.

5. Conclusions

In the present study, the irradiation response of equiatomic Cr-FeMnNi and AlCrFeMnNi under 5 MeV Fe^{2+} ion at 500 °C to a peak fluence of 50 and 100 dpa have been examined. Both alloys exhibited extraordinary phase stability under ion irradiation. CrFeMnNi HEA contains dominant FCC phase with limited Cr enriched α' particles, and AlCrFeMnNi presents BCC FeCrMn-rich matrix with a B2 AlNi-rich second phase, in which FeCrMn-rich nanoprecipitates with an average diameter of 27 nm were found. In dual-phase AlCrFeMnNi, no RIS was detected after irradiation, however the width of the interface tends to be larger with increasing irradiation dose. Void formation was observed in both irradiated alloys. In CrFeMnNi, limited voids (6 nm voids with a density of $1.5 \times 10^{21}/m^3$, corresponding to approximate 0.017% local volume fraction) were only detected at the peak damage location of ~ 50 dpa, while voids were widely distributed in AlCr-FeMnNi. Under both 50 and 100 peak dpa irradiation conditions, voids were found with larger dimensions and a denser distribution in the FeCrMn-rich matrix, and a smaller and slightly lower density in the AlNi-rich second phase. From the analysis of size distribution, FeCrMn-rich nanoprecipitates didn't reveal any tendency to dissolve or grow after irradiation with peak doses of 50 and 100 dpa. Nanoindentation experiments have uncovered a dramatic hardness increase (0.9 GPa corresponding to 24% hardening) in CrFeMnNi after ion irradiation, but only $\sim 4\%$ hardness increase (from 7.4 to 7.7 GPa) in dual-phase AlCrFeMnNi. The discrepancy of hardening models and the radiation induced defect formation indicates that besides radiation induced defects such as voids, dislocation loops and point defects, the role of other effects such as chemical short-range ordering will need to be explored in future work.

Declaration of competing interest

The authors declare that they have no known competing financial interests or personal relationships that could have appeared to influence the work reported in this paper.

The authors declare the following financial interests/personal relationships which may be considered as potential competing interests:

CRediT authorship contribution statement

Youxing Chen: Conceptualization, Writing – original draft. **Di Chen:** Methodology, Investigation, Writing – review & editing. **Jordan Weaver:** Investigation, Writing – review & editing. **Jonathan Gigax:** Investigation, Writing – review & editing. **Yongqiang Wang:** Methodology, Writing – review & editing. **Nathan A. Mara:** Writing – review & editing. **Saryu Fensin:** Writing – review & editing, Funding acquisition. **Stuart A. Maloy:** Writing – review & editing, Funding acquisition. **Amit Misra:** Writing – review & editing, Conceptualization. **Nan Li:** Conceptualization, Writing – original draft, Supervision, Funding acquisition.

Data availability

Data will be made available on request.

Acknowledgments

The authors acknowledge the support of the Los Alamos National Laboratory (LANL)/Laboratory Directed Research & Development (LDRD) and Institute for Materials Science (IMS) Program. This work was performed, in part, at the Center for Integrated Nanotechnologies, an Office of Science User Facility operated for the U.S. Department of Energy (DOE) Office of Science. Los Alamos National Laboratory, an affirmative action equal opportunity employer, is operated by Triad National Security, LLC, for the National Nuclear Security Administration of the U.S. DOE under contract 89233218CNA000001.

References

- [1] DOENext Generation Materials: Technology Assessment, DOE, 2015.
- [2] S.J. Zinkle, L.L. Snead, Designing radiation resistance in materials for fusion energy, *Annu. Rev. Mater. Res.* 44 (2014) 241–267.
- [3] A. Peakman, Z. Hodgson, B. Merk, Advanced micro-reactor concepts, *Prog. Nucl. Energy* 107 (2018) 61–70.
- [4] H. Bolt, V. Barabash, W. Krauss, J. Linke, R. Neu, S. Suzuki, N. Yoshida, A.U. Team, Materials for the plasma-facing components of fusion reactors, *J. Nucl. Mater.* 329 (2004) 66–73.
- [5] G.S. Was, Fundamentals of radiation materials science: metals and alloys, Springer2016.
- [6] Z. Li, S. Zhao, R.O. Ritchie, M.A. Meyers, Mechanical properties of high-entropy alloys with emphasis on face-centered cubic alloys, *Prog. Mater. Sci.* 102 (2019) 296–345.
- [7] Y. Zhang, T.T. Zuo, Z. Tang, M.C. Gao, K.A. Dahmen, P.K. Liaw, Z.P. Lu, Microstructures and properties of high-entropy alloys, *Prog. Mater. Sci.* 61 (2014) 1–93.
- [8] B. Gludovatz, A. Hohenwarter, D. Catoor, E.H. Chang, E.P. George, R.O. Ritchie, A fracture-resistant high-entropy alloy for cryogenic applications, *Science* 345 (6201) (2014) 1153–1158.
- [9] D.B. Miracle, O.N. Senkov, A critical review of high entropy alloys and related concepts, *Acta Mater.* 122 (2017) 448–511.
- [10] J. He, W. Liu, H. Wang, Y. Wu, X. Liu, T. Nieh, Z. Lu, Effects of Al addition on structural evolution and tensile properties of the FeCoNiCrMn high-entropy alloy system, *Acta Mater.* 62 (2014) 105–113.
- [11] Z. Li, K.G. Pradeep, Y. Deng, D. Raabe, C.C. Tasan, Metastable high-entropy dual-phase alloys overcome the strength-ductility trade-off, *Nature* 534 (7606) (2016) 227–230.
- [12] E.P. George, D. Raabe, R.O. Ritchie, High-entropy alloys, *Nature Rev. Mater.* 4 (8) (2019) 515–534.
- [13] K. Ming, L. Li, Z. Li, X. Bi, J. Wang, Grain boundary decohesion by nanoclustering Ni and Cr separately in CrMnFeCoNi high-entropy alloys, *Sci. Adv.* 5 (12) (2019) eaay0639.
- [14] D. Chen, Y. Tong, H. Li, J. Wang, Y. Zhao, A. Hu, J. Kai, Helium accumulation and bubble formation in FeCoNiCr alloy under high fluence He+ implantation, *J. Nucl. Mater.* 501 (2018) 208–216.
- [15] Z. Yan, S. Liu, S. Xia, Y. Zhang, Y. Wang, T. Yang, He behavior in Ni and Ni-based equiatomic solid solution alloy, *J. Nucl. Mater.* 505 (2018) 200–206.
- [16] Z. Fan, S. Zhao, K. Jin, D. Chen, Y.N. Osetsky, Y. Wang, H. Bei, K.L. More, Y. Zhang, Helium irradiated cavity formation and defect energetics in Ni-based binary single-phase concentrated solid solution alloys, *Acta Mater.* 164 (2019) 283–292.
- [17] Y. Zhang, X. Wang, Y.N. Osetsky, Y. Tong, R. Harrison, S.E. Donnelly, D. Chen, Y. Wang, H. Bei, B.C. Sales, Effects of 3d electron configurations on helium bubble formation and void swelling in concentrated solid-solution alloys, *Acta Mater.* 181 (2019) 519–529.
- [18] T. Yang, C. Li, S.J. Zinkle, S. Zhao, H. Bei, Y. Zhang, Irradiation responses and defect behavior of single-phase concentrated solid solution alloys, *J. Mater. Res.* 33 (19) (2018) 3077–3091.
- [19] Y. Zhang, S. Zhao, W.J. Weber, K. Nordlund, F. Granberg, F. Djurabekova, Atomic-level heterogeneity and defect dynamics in concentrated solid-solution alloys, *Curr. Opin. Solid State Mater. Sci.* 21 (5) (2017) 221–237.
- [20] O. El-Atwani, N. Li, M. Li, A. Devaraj, J. Baldwin, M.M. Schneider, D. Sobieraj, J.S. Wróbel, D. Nguyen-Manh, S.A. Maloy, Outstanding radiation resistance of tungsten-based high-entropy alloys, *Sci. Adv.* 5 (3) (2019) eaav2002.
- [21] Y. Zhang, Y.N. Osetsky, W.J. Weber, Tunable Chemical Disorder in Concentrated Alloys: defect Physics and Radiation Performance, *Chem. Rev.* 122 (1) (2021) 789–829.
- [22] Y. Zhang, G.M. Stocks, K. Jin, C. Lu, H. Bei, B.C. Sales, L. Wang, L.K. Béland, R.E. Stoller, G.D. Samolyuk, Influence of chemical disorder on energy dissipation and defect evolution in concentrated solid solution alloys, *Nat. Commun.* 6 (2015) 8736.
- [23] Z. Wang, C. Liu, P. Dou, Thermodynamics of vacancies and clusters in high-entropy alloys, *Phys. Rev. Mater.* 1 (4) (2017) 043601.
- [24] C. Lu, L. Niu, N. Chen, K. Jin, T. Yang, P. Xiu, Y. Zhang, F. Gao, H. Bei, S. Shi, Enhancing radiation tolerance by controlling defect mobility and migration pathways in multicomponent single-phase alloys, *Nat. Commun.* 7 (1) (2016) 1–8.
- [25] S. Zhao, Y. Osetsky, A.V. Barashev, Y. Zhang, Frenkel defect recombination in Ni and Ni-containing concentrated solid-solution alloys, *Acta Mater.* 173 (2019) 184–194.
- [26] D.S. Aidhy, C. Lu, K. Jin, H. Bei, Y. Zhang, L. Wang, W.J. Weber, Point defect evolution in Ni, NiFe and NiCr alloys from atomistic simulations and irradiation experiments, *Acta Mater.* 99 (2015) 69–76.
- [27] M.W. Ullah, D.S. Aidhy, Y. Zhang, W.J. Weber, Damage accumulation in ion-irradiated Ni-based concentrated solid-solution alloys, *Acta Mater.* 109 (2016) 17–22.
- [28] F. Granberg, K. Nordlund, M.W. Ullah, K. Jin, C. Lu, H. Bei, L. Wang, F. Djurabekova, W. Weber, Y. Zhang, Mechanism of radiation damage reduction in equiatomic multicomponent single phase alloys, *Phys. Rev. Lett.* 116 (13) (2016) 135504.
- [29] C. Lu, T. Yang, K. Jin, N. Gao, P. Xiu, Y. Zhang, F. Gao, H. Bei, W.J. Weber, K. Sun, Radiation-induced segregation on defect clusters in single-phase concentrated solid-solution alloys, *Acta Mater.* 127 (2017) 98–107.
- [30] C.M. Barr, J.E. Nathaniel II, K.A. Unocic, J. Liu, Y. Zhang, Y. Wang, M.L. Taheri, Exploring radiation induced segregation mechanisms at grain boundaries in equiatomic CoCrFeNiMn high entropy alloy under heavy ion irradiation, *Scr. Mater.* 156 (2018) 80–84.
- [31] N.K. Kumar, C. Li, K. Leonard, H. Bei, S. Zinkle, Microstructural stability and mechanical behavior of FeNiMnCr high entropy alloy under ion irradiation, *Acta Mater.* 113 (2016) 230–244.
- [32] M.-R. He, S. Wang, S. Shi, K. Jin, H. Bei, K. Yasuda, S. Matsumura, K. Higashida, I.M. Robertson, Mechanisms of radiation-induced segregation in Cr-FeCoNi-based single-phase concentrated solid solution alloys, *Acta Mater.* 126 (2017) 182–193.
- [33] V. Soare, M. Burada, I. Constantin, D. Mitrică, V. Bădiliță, A. Caragea, M. Tărcolea, Electrochemical deposition and microstructural characterization of AlCr-FeMnNi and AlCrCuFeMnNi high entropy alloy thin films, *Appl. Surf. Sci.* 358 (2015) 533–539.
- [34] A. Munitz, L. Meshi, M. Kaufman, Heat treatments' effects on the microstructure and mechanical properties of an equiatomic Al-Cr-Fe-Mn-Ni high entropy alloy, *Mater. Sci. Eng.: A* 689 (2017) 384–394.
- [35] N. Stepanov, D. Shaysultanov, M. Tikhonovsky, G. Salishchev, Tensile properties of the Cr-Fe-Ni-Mn non-equiatomic multicomponent alloys with different Cr contents, *Mater. Des.* 87 (2015) 60–65.
- [36] T. Yang, S. Xia, W. Guo, R. Hu, J.D. Poplawsky, G. Sha, Y. Fang, Z. Yan, C. Wang, C. Li, Effects of temperature on the irradiation responses of Al0.1CoCrFeNi high entropy alloy, *Scr. Mater.* 144 (2018) 31–35.
- [37] B. Kombaiah, K. Jin, H. Bei, P.D. Edmondson, Y. Zhang, Phase stability of single phase Al0.12CrNiFeCo high entropy alloy upon irradiation, *Mater. Des.* 160 (2018) 1208–1216.
- [38] S. Xia, X. Yang, T. Yang, S. Liu, Y. Zhang, Irradiation resistance in Al x CoCrFeNi high entropy alloys, *JOM* 67 (10) (2015) 2340–2344.
- [39] S. Xia, M.C. Gao, T. Yang, P.K. Liaw, Y. Zhang, Phase stability and microstructures of high entropy alloys ion irradiated to high doses, *J. Nucl. Mater.* 480 (2016) 100–108.
- [40] P.K. Liaw, T. Egami, C. Zhang, F. Zhang, ... Y. Zhang, Radiation Behavior of High-Entropy Alloys for Advanced Reactors, Univ. of Tennessee, Knoxville, TN (United States), 2015 Final report.
- [41] J.F. Ziegler, M.D. Ziegler, J.P. Biersack, SRIM-The stopping and range of ions in matter, *Nucl. Instrum. Method. Phys. Res. Sect. B* 268 (11–12) (2010) 1818–1823.
- [42] S.J. Zinkle, J.T. Busby, Structural materials for fission & fusion energy, *Mater. Today* 12 (11) (2009) 12–19.
- [43] W.C. Oliver, G.M. Pharr, Measurement of hardness and elastic modulus by instrumented indentation: advances in understanding and refinements to methodology, *J. Mater. Res.* 19 (1) (2004) 3–20.
- [44] J.G. Gigax, O. El-Atwani, Q. McCulloch, B. Ayutina, M. Efe, S. Fensin, S.A. Maloy, N. Li, Micro-and mesoscale mechanical properties of an ultra-fine grained Cr-FeMnNi high entropy alloy produced by large strain machining, *Scr. Mater.* 178 (2020) 508–512.
- [45] Y. Chen, E. Hintsala, N. Li, B.R. Becker, J.Y. Cheng, B. Nowakowski, J. Weaver, D. Stauffer, N.A. Mara, High-throughput Nanomechanical screening of phase-specific and temperature-dependent hardness in Al x FeCrNiMn High-Entropy Alloys, *JOM* 71 (10) (2019) 3368–3377.
- [46] D.A. Porter, K.E. Easterling, M. Sherif, Phase Transformations in Metals and Alloys (revised reprint), CRC press, 2009.
- [47] C.-J. Tong, Y.-L. Chen, J.-W. Yeh, S.-J. Lin, S.-K. Chen, T.-T. Shun, C.-H. Tsau, S.-Y. Chang, Microstructure characterization of Al x CoCrCuFeNi high-entropy alloy system with multiprincipal elements, *Metallurgic. Mater. Trans. A* 36 (4) (2005) 881–893.
- [48] S. Singh, N. Wanderka, B. Murty, U. Glatzel, J. Banhart, Decomposition in multi-component AlCoCrCuFeNi high-entropy alloy, *Acta Mater.* 59 (1) (2011) 182–190.
- [49] A. Misra, R. Gibala, Room-temperature deformation behavior of directionally solidified multiphase Ni-Fe-Al alloys, *Metallurgic. Mater. Trans. A* 28 (3) (1997) 795–807.
- [50] R. Li, W. Zhang, Y. Zhang, P.K. Liaw, The effects of phase transformation on the microstructure and mechanical behavior of FeNiMnCr_75Alx high-entropy alloys, *Mater. Sci. Eng.: A* 725 (2018) 138–147.
- [51] C. Sun, M. Kirk, M. Li, K. Hattar, Y. Wang, O. Anderoglu, J. Valdez, B. Uberuaga, R. Dickerson, S. Maloy, Microstructure, chemistry and mechanical properties

- of Ni-based superalloy Rene N4 under irradiation at room temperature, *Acta Mater.* 95 (2015) 357–365.
- [52] T. Lee, A. Caro, M.J. Demkowicz, Atomistic modeling of radiation-induced disordering and dissolution at a Ni/Ni 3 Al interface, *J Mater Res* 30 (9) (2015) 1456–1463.
- [53] G. Lucas, The evolution of mechanical property change in irradiated austenitic stainless steels, *J. Nucl. Mater.* 206 (2–3) (1993) 287–305.
- [54] S. Zinkle, Fundamental radiation effects parameters in metals and ceramics, *Radiat Eff. Defects Solids* 148 (1–4) (1999) 447–477.
- [55] N. Li, M. Nastasi, A. Misra, Defect structures and hardening mechanisms in high dose helium ion implanted Cu and Cu/Nb multilayer thin films, *Int. J. Plast.* 32 (2012) 1–16.
- [56] X. Zhang, K. Hattar, Y. Chen, L. Shao, J. Li, C. Sun, K. Yu, N. Li, M.L. Taheri, H. Wang, Radiation damage in nanostructured materials, *Prog. Mater Sci.* 96 (2018) 217–321.
- [57] N. Li, M. Demkowicz, N. Mara, Y. Wang, A. Misra, Hardening due to interfacial He bubbles in nanolayered composites, *Mater. Res. Lett.* 4 (2) (2016) 75–82.
- [58] Q. Wei, N. Li, N. Mara, M. Nastasi, A. Misra, Suppression of irradiation hardening in nanoscale V/Ag multilayers, *Acta Mater.* 59 (16) (2011) 6331–6340.
- [59] R. Stoller, S. Zinkle, On the relationship between uniaxial yield strength and resolved shear stress in polycrystalline materials, *J. Nucl. Mater.* 283 (2000) 349–352.
- [60] L. Tan, J.T. Busby, Formulating the strength factor α for improved predictability of radiation hardening, *J. Nucl. Mater.* 465 (2015) 724–730.
- [61] R. Zhang, S. Zhao, J. Ding, Y. Chong, T. Jia, C. Ophus, M. Asta, R.O. Ritchie, A.M. Minor, Short-range order and its impact on the CrCoNi medium-entropy alloy, *Nature* 581 (7808) (2020) 283–287.
- [62] S. Wang, X. Liu, Z. Lei, D. Lin, F. Bian, C. Yang, M. Jiao, Q. Du, H. Wang, Y. Wu, Chemical short-range ordering and its strengthening effect in refractory high-entropy alloys, *Phys. Rev. B* 103 (10) (2021) 104107.
- [63] S. Chen, Z.H. Aitken, S. Pattamatta, Z. Wu, Z.G. Yu, D.J. Srolovitz, P.K. Liaw, Y.-W. Zhang, Simultaneously enhancing the ultimate strength and ductility of high-entropy alloys via short-range ordering, *Nat. Commun.* 12 (1) (2021) 1–11.
- [64] A. Konno, N.H. Oono, S. Ukai, S. Kondo, O. Hashitomi, A. Kimura, Stability of γ' precipitates in nickel based oxide dispersion-strengthened Superalloys under high-temperature and heavy irradiation conditions, *Mater. Trans.* (2019) M2019050.
- [65] R. Nelson, J. Hudson, D. Mazey, The stability of precipitates in an irradiation environment, *J. Nucl. Mater.* 44 (3) (1972) 318–330.
- [66] C. Varvenne, A. Luque, W.A. Curtin, Theory of strengthening in fcc high entropy alloys, *Acta Mater.* 118 (2016) 164–176.